Thermal desorption of H₂O ice: from nanoscale films to the bulk

Alexander Rosu-Finsen ®,★ Bharvi Chikani and Christoph G. Salzmann
Department of Chemistry, University College London, 20 Gordon Street WC1H 0AJ, London, UK

ABSTRACT

The desorption properties of H₂O films are investigated across a wide range of film thicknesses from 53 nanometres (nm) to 101 micrometres (μm) using a quartz-crystal microbalance (QCM) and temperature-programmed desorption. Three desorption stages are observed belonging to amorphous solid water (ASW), stacking disordered ice I (ice Isd), and hexagonal ice I (ice Ih). The desorption of ASW is only detectable for the ≥ 10 μm films and is separated from the ice I desorption by 10–15 K with an associated desorption energy of ~ 64 kJ mol^{-1}. The desorption energy of the 53-nm film was found to be near 50 kJ mol^{-1} as also noted in the literature, but with increasing film thickness, the desorption energy of ice I rises, reaching a plateau around 65–70 kJ mol^{-1}. The reason for the increased desorption energy is suggested to be due to molecules unable to desorb due to the thick covering layer of H₂O and possibly re-adsorption events. Before complete desorption of ice I at around 220 K for the 101 μm film, a two-stage ice I desorption is observed with the QCM for the ≥ 10 μm films near 200 K. This event corresponds to the desorption of ice Isd as corroborated by X-ray diffraction patterns collected upon heating from 92 to 260 K at ambient pressure. Cubic ice is not observed as is commonly stated in the literature as resulting from the crystallization of ASW. Therefore, ice Isd is the correct terminology for the initial crystallization product of ASW.

Key words: astrochemistry – ISM: molecules – methods: laboratory: molecular – methods: laboratory: solid state.

1 INTRODUCTION

Amorphous solid water (ASW) was discovered in the 1930s by vapour deposition onto a cryogenically cooled copper substrate (Burton & Oliver 1935a, 1935b). ASW is a type of low-density amorphous (LDA) ice, but LDA can be made via different methods such as decompression or heating of high-density amorphous (HDA) ice (Mishima, Calvert & Whalley 1984, 1985). The notion of LDA-I and LDA-II was brought forward when differently treated HDA ices were transformed to LDA and analysed through diffraction (Winkel et al. 2009), but vibrational spectroscopic measurements were not able to distinguish the difference between such LDA types (Shephard, Evans & Salzmann 2013). LDA can also be made by rapidly cooling liquid water-droplets, forming hyperquenched glassy water (Brüggeller & Mayer 1980; Mayer & Brüggeller 1982), or when ice VIII is heated at ambient pressure (Klug et al. 1989). Interestingly, spectroscopy can distinguish between LDA from ice VIII and other LDA ices (Shephard et al. 2016).

Depending on the preparation conditions such as molecular beam or background dosing, deposition rate, and angle, the morphology of ASW is significantly affected (Mayer & Pletzer 1984; Stevenson et al. 1999; Kimmel et al. 2001; Dohnálek et al. 2002). Another important parameter to control is the temperature where porous or compact ASW form depending on the substrate temperature (Narten, Venkatesh & Rice 1976; Jenniskens & Blake 1994). It is important to note that the high-density vapour-deposited polyamorph is not similar to the compressed high-density amorphous ice (Mishima et al. 1984). Regardless of the morphology and density of ASW, this polyamorph is the most abundant solid-state material in the interstellar medium (Williams, Fraser & McCoustra 2002; Tielens 2013) where reactive accretion onto dust grains in dark molecular clouds is the main formation pathway (Linnartz, Ioppolo & Fedoseev 2015).

As highlighted recently (Potapov, Jäger & Henning 2020), based on H₂O column densities (Gibb et al. 2004; Boogert et al. 2008; Boogert et al. 2011), it was estimated that 300–12,000 monolayers (ML) can be present on interstellar dust grains. With a bulk density of LDA of 0.93 g cm^{-3} (Mishima, Calvert & Whalley 1985), these layers can be estimated as being about 90–360 nm thick. Boogert et al. also mention a column density for a young stellar object, IRAS 03245 + 3002, being nearly 4×10^{19} cm^{-2}, leading to ice thicknesses of about 1.2 μm (Boogert et al. 2008). Interstellar dust grains range in size from the nanometre to micrometre level (Mathis, Rumpl & Nordsieck 1977) and an ice coating of similar thickness is reasonable to consider for individual grains in dense interstellar media, which matches the approximate thicknesses mentioned above. Icy, sticky dust grains coagulate, forming larger particles and ultimately comets and asteroids (Wada et al. 2009; Gundlach & Blum 2014). As the size of particles, comets, and asteroids grow, so too can ice grow beyond the nanometre and micrometre thicknesses. Micrometre-sized ice particles have been studied regarding their viscosity or 'stickiness' (Gundlach & Blum 2014), where e.g. the agglomeration of particles in the Saturnian rings has been suspected to be greatly aided if micrometre-thick films H₂O-ice are present (Hatzes et al. 1991). Further to this, the collisional properties of centimetre-sized

ice particles are of interest to Saturn's rings (McDonald et al. 1989; Heißelmann et al. 2010). Such collisional experimental information is also relevant for protoplanetary discs where millimetre-sized particles have been investigated (Aumatell & Wurm 2011; Hill et al. 2015; Gärtner et al. 2017). Ices of vastly greater thicknesses ranging from metres to kilometres have also been estimated on a range of objects such as comets, satellites, and planets (De Sanctis et al. 2015; Filacchione et al. 2016; Grundy et al. 2016).

Agglomerated comets and asteroids may be highly porous where a range of high-energy binding sites can be present. Recent experiments of H_2O physisorbed onto highly porous silicate grain material showed a drastic delay in desorption up to 200 K (Potapov et al. 2021). Likewise, H_2O mixed with C_{60}-fullerenes (Halukeerthi et al. 2020) and fullerene-like carbon grains (Potapov, Jäger & Henning 2018) have shown suppression or delays in desorption. The change in H_2O desorption behaviour is believed to occur as the percolation threshold of the guest species is approached (Halukeerthi et al. 2020), and a similar concentration-dependent behaviour has been noted in the photodesorption of H_2O-antracoronene mixtures (Korsmeyer et al. 2022).

Sub-ML coverages of H_2O have been shown to produce clusters (Carrasco, Hodgson & Michaelides 2012; Rosu-Finsen et al. 2016; Marchione et al. 2019), explaining why H_2O desorption commonly occurs through zero-order kinetics (Collings et al. 2001; Fraser et al. 2001; Smith, Matthiesen, and Kay 2014; Collings et al. 2015). ASW is a porous material (Mitterdorfer et al. 2014; Hill et al. 2016), and recent experiments have proposed that the collapse of such pores near 120–130 K constitutes a new desorption pathway for trapped guest species only seen in thick ASW films (Talewar et al. 2019). Common for both thin and thick ASW films with guest species is the expulsion of guests during crystallization (Collings et al. 2003, 2004; Talewar et al. 2019) that has been termed the molecular volcano (Smith et al. 1997; May, Smith & Kay 2012). Since pure H_2O desorption has been shown to peak as high as 180 K (depending on heating rate and film thickness), the ASW sublimation feature during crystallization usually overlaps with the overall H_2O desorption profile (Collings et al. 2001; Fraser et al. 2001; Smith, Matthiesen & Kay 2014; Collings et al. 2015).

When considering interstellar H_2O-ice, the conditions afforded by an ultrahigh vacuum system are ideal. However, as dust grains agglomerate into larger structures, the ice thicknesses will increase, and ultrahigh vacuum systems do not cope well with desorption of large quantities of adsorbates. In this work, we combine a quartz-crystal microbalance (QCM) with temperature-programmed desorption (TPD) to explore the sublimation behaviour of H_2O films spanning from 53 nm to 101 μm in a high-vacuum chamber. With such bulk materials, we also study the transition of ASW to hexagonal/cubic stacking disordered ice I (ice Isd), as well as the final formation of the stable hexagonal ice I (ice Ih) through ambient pressure X-ray diffraction.

2 EXPERIMENTAL

The general workings of the experimental equipment and analytical methods used in this work have been detailed previously (Talewar et al. 2019; Halukeerthi et al. 2020), however, a specific description of the experimental procedure follows here.

A diffusion pump (Diffstak 63/150 M, BOC Edwards) with a pumping speed of 135 L s^{-1} backed by a rotary pump (model 12, BOC Edwards) and a liquid nitrogen cooled trap is used to routinely achieve a base pressure of $< 2 \times 10^{-7}$ mbar in a high-vacuum chamber (Kurt J. Lesker Ltc., $12 \times 12 \times 24$ inch internal dimension) as

Table 1. Experimental heating rates during desorption that vary with the amount of deposited H_2O.

Film thickness	Heating rate/K min^{-1}
53 nm	0.43
100 nm	0.45
210 nm	0.45
500 nm	0.47
2 μm	0.50
10 μm	0.73
20 μm	0.82
51 μm	0.89
101 μm	0.92

measured by a dual combination cold cathode/Pirani pressure gauge (PenningVac PTR 90, Oerlikon Leybold Vacuum). An inlet tube covered with a metal mesh attached to a high-precision needle valve (EV 016 DOS AB, Oerlikon Leybold Vacuum) controlled the amount of ultrapure H_2O (MiliQ, Milipore) vapour allowed into the chamber at a constant pressure. Before use, the H_2O was further purified by several freeze-pump-thaw cycles. A liquid nitrogen cooled 8-inch diameter copper deposition substrate placed 15 cm from the inlet tube (but positioned in-line) routinely reaches a base temperature of 84 $\pm$ 1 K as measured by a K-type thermocouple attached to the edge of the deposition plate and connected to a purpose-made temperature read-out unit containing an Adafruit Feather 32u4 Basic Proto microcontroller and an Adafruit MAX31856 Universal Thermocouple Amplifier. At this distance, deposited films are as flat as possible, considering the deposition conditions as previously determined through quartz crystal microbalance (QCM) measurements performed radially across the deposition plate (Talewar et al. 2019). When desired, the deposition plate can be removed from the vacuum chamber once an icy film has been deposited for further *ex situ* analysis at ambient pressure (1 atmosphere). Attached to the deposition plate is a QCM fitted with a gold-plated AT-cut 6 MHz planoconvex quartz crystal placed inside an Allectra 710-SH sensor. The QCM sensor was connected to a reflection bridge and a 0.5–60 MHz N2PK vector network analyser collecting data points every 2.5 s. The QCM was used to monitor the film thickness in real time and deposition ceased once a desired film thickness was achieved. During deposition at 84 K, the chamber pressure reached $\sim 1 \times 10^{-5}$ mbar, which was kept constant and only the deposition time was altered to allow for the varying film thicknesses. TPD was recorded by a residual gas analyser mass spectrometer (Hiden Analytical, HALO 201) monitoring the partial pressures in the 10–35 *m/z* range. N_2 was determined to be the main trace-gas with a partial pressure of 1×10^{-8} mbar. During ASW deposition, trace amounts of N_2 were trapped in the ASW films, however, this was deemed inconsequential to the ASW and ice I desorption kinetics as discussed in section 1 of the SI and shown in Fig. S1. The deposition plate was heated by simply stopping the cooling system that is composed of a membrane pump sucking cold gas from a liquid nitrogen reservoir through the cryostat. From Fig. S2, the individual heating rates can be seen as being linear during H_2O desorption where the gradient of the linear fits, marked in red, indicate the heating rates shown in Table 1.

An experiment involving a recovered ASW sample was also conducted. Following ASW deposition, the ice was annealed at 125 K to close the pores of ASW and prevent N_2 hydrate formation when extracting the sample with liquid nitrogen at ambient pressure (Mayer & Hallbrucker 1989). The ASW was transferred into a custom-made 1 mm thick brass X-ray sample holder with a 3×9 mm hole cut into the metal to which a 0.025 mm Kapton foil was glued

to and enclosed with a Kapton-windowed lid under liquid nitrogen conditions. The filled sample holder was mounted on a Stoe Stadi P X-ray diffractometer with Cu K$_\alpha$1 radiation at 40 kV, 30 mA and monochromated by a Ge 111 crystal. The temperature of the ASW was controlled by an Oxford Instruments CryoJetHT. X-ray diffraction patterns were collected by a Mythen 1 K detector over 25-min intervals at a base temperature of 92 K and then in 10 K steps from 100 K until the melt with a 1 K min^{-1} heating rate. The sample holder was not hermetically sealed, but an N$_2$(g) shield gas from the CryoJetHT prevented the formation of condensed ice during data collection.

3 RESULTS AND DISCUSSIONS

3.1 Quartz crystal microbalance

Fig. 1(a) shows the decrease in frequency as ASW is deposited onto the QCM crystal. Since the inlet pressure is kept constant, the change in frequency (Δf) is mainly linear as seen in Fig. 1(a) where the change in mass (Δm) of H$_2$O deposited on the QCM crystal can be calculated from the Sauerbrey equation, equation (1),

$$\Delta f = -\frac{2f_0^2}{A\sqrt{\rho_q \mu_q}} \times \Delta m \qquad (1)$$

where f_0 is the resonant frequency of the crystal, A is the active crystal area, and ρ_q and μ_q are the density and shear modulus of quartz, respectively. With increasing film thickness, the frequency change becomes larger, reaching a point where small deviations from the Sauerbrey equation are observed. This is due to the influence of viscoelastic effects that become important when the film thickness is a sizeable fraction of the wavelength of the shear sound (Talewar et al. 2019). Small negative deviations from the Sauerbrey equation, which predicts a linear frequency change for constant deposition rates, can be seen towards the end of the depositions of the 51 and 101 μm films in Fig. 1(a) highlighted with the black arrows. With the limitations of equation (1) in mind leading to the non-linearity in Fig. 1(a), we estimated the film thicknesses as shown in Table 2 based on the mass determined from equation (1) and the bulk density of ASW (0.93 g cm^{-3}; Mishima et al. 1985). Performing linear extrapolations of the frequency changes towards the ends of the deposition experiments, estimated film thicknesses of 45 and 86 μm are obtained for the nominally 51 and 101 μm films, respectively.

The porosity of ASW at ∼80 K has previously been studied through small-angle scattering upon deposition as well as heating where pores continuously change shape above ∼120 K (Mitterdorfer et al. 2014; Hill et al. 2016; Li et al. 2021). Scanning electron microscopy and nuclear magnetic resonance have also been used to investigate the porosity of ASW (Lisitsin-Baranovsky et al. 2016). Pore formation is not observed upon deposition, nor is pore collapse observed upon heating, however, observing such events with QCM is not expected. Following deposition, the amorphous ice was heated with the QCM monitoring the desorption as shown in Figs 1(b) and (c) of the adjacent-averaged smoothed derivative of the QCM signal (df/dt). Near 150 K, ASW desorbs as the free energy of ASW is greater than that of its crystalline form (Kouchi 1987; Sack & Baragiola 1993; Smith et al. 2012; Nachbar, Duft & Leisner 2018) leading to a greater vapour pressure of ASW. As such, crystallization, in essence, prevents the full desorption of ASW resulting in the desorption peak in panel (c) for the 51 and 101 μm films. Desorption features of guest species in an ASW matrix in this temperature region are typically termed molecular volcano (Smith et al. 1997; May,
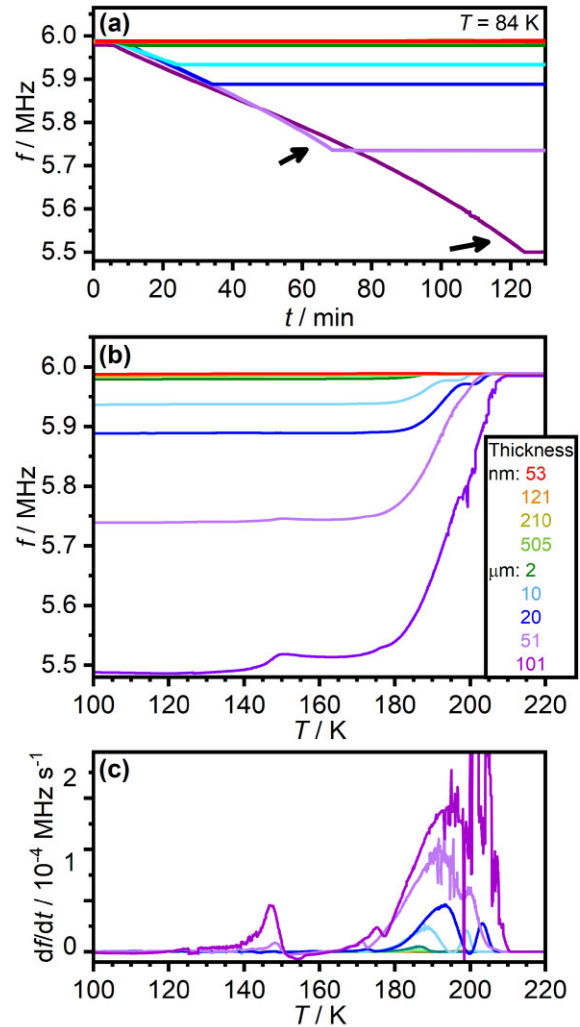

Figure 1. (a) Decrease in frequency during ASW deposition at 84 K. The arrows highlight the small deviations from the Sauerbrey equation for the 51 and 101 μm films. (b) Frequency changes upon heating H$_2$O films of increasing thicknesses. (c) Differentiated and 25-point adjacent-averaged smoothed QCM signal with respect to time but plotted against temperature. Loss of mass is noted at 150 K for the 51 and 101 μm films, and full ice I desorption through a two-stage process starting near 170 and 200 K depending on film thickness. The colour legend in panel (b) is valid for all panels.

Table 2. Overall frequency changes upon deposition used to determine the mass of H$_2$O deposited onto the entire plate. The film thicknesses and numbers of ML are calculated using the mass and density of ASW.

Δf/Hz	Δm/mg	Film thickness	H$_2$O monolayers/ML
−261	2	53 nm	178
−593	4	121 nm	405
−1021	6	209 nm	698
−2464	15	505 nm	1684
−11 012	51	2 μm	7526
−50 127	309	10 μm	34 258
−98 193	606	20 μm	67 108
−250 414	1545	51 μm	171 140
−494 690	3051	101 μm	338 084

Smith & Kay [2012]). However, the desorption events in this work belong purely to H_2O and are therefore not the typical molecular volcano, but simply desorption of ASW. As this technique concerns frequency changes due to variations in mass, the loss of H_2O can be quantified at ∼4 percent for the 101 μm film. It is interesting to note that the 101 μm films exhibit a desorption feature greater than double that of the 51 μm film, while thinner films exhibit no desorption feature near 150 K, indicating that a threshold has been crossed between 20 and 51 μm. Since H_2O is known to have poor thermal conductivity (Kouchi et al. [1992]), it is possible that the exothermic nature of crystallization leads to local heating predominately at the surface of the thickest film, thereby increasing the desorption rate and yielding an observable QCM desorption feature near 150 K. Alternatively, since the 101 and 51 μm films showed negative deviations from the Sauerbrey equation towards the end of the deposition, it is possible that the compaction of the films or other morphology changes during crystallization restore Sauerbrey behaviour with associated increases of frequency. This scenario would mean that mass losses during the crystallization of ASW are generally difficult to capture with QCM.

Following crystallization, a slight decrease in frequency can be seen in Fig. [1](b) and a drop below the baseline in panel (c). This frequency decrease has previously been observed (Talewar et al. 2019) and discussed as possibly arising due to the release of bending stresses.

A two-stage desorption event for ice I is clearly seen in panel (c) for the $>10\mu$m films at around 200 K, which indicates the possible transition from one solid-state species to another with different vapour pressures and coincides with the ice Isd to ice Ih transition (Kuhs, Bliss & Finney [1987]; Malkin et al. [2015]). Ice Isd is metastable with respect to ice Ih and has a higher free energy and therefore a higher vapour pressure meaning ice Isd desorbs at a lower temperature. Unfortunately, the changes in mass occur rapidly >190 K, meaning the resonant frequency of the QCM crystal is sometimes lost, which leads to the noisy data especially seen for the 51 and 101 μm data where mass changes are the fastest. Following the ice Ih desorption, the QCM signal reaches 6 MHz, indicating that the crystal and deposition plate are once again bare. In the case of the thinner films, complete desorption is achieved before the ice Isd to ice Ih phase transition is even observed.

3.2 X-ray diffraction of vapour-deposited H_2O

The ice I family is comprised of structures ranging from only hexagonal stacking, called ice Ih, to the entirely cubic stacking in ice I (ice Ic). Between these end-members is what has been termed ice Isd (Kuhs et al. [2012]; Malkin et al. [2015]), along with a range of more complex and periodic stacking sequences such as the 4H, 6H, and 9R polytypes (Salzmann & Murray [2020]). Simulated diffraction patterns of the ice I polytypes can be found in the supplementary information, Fig. S3. Ice Ih is the thermodynamically stable phase of ice at ambient pressure, hence all phases of ice eventually transform to this with increasing temperature. In the literature, the erroneous description of ASW transforming to ice Ic at 150 K followed by an ice Ic→Ih transition at higher temperatures is commonplace. Ice Ic has only recently been prepared in its pure form, following complex preparation procedures (del Rosso et al. [2020]; Komatsu et al. [2020]).

To illustrate the transformation of ASW to ice Isd, Fig. [2](a) shows the X-ray diffraction data (in black) upon heating ASW at ambient pressure from 92 to 260 K.

The experimental data in Fig. [2](a) was obtained from a 101 μm ASW film prepared in the vacuum chamber and extracted to ambient
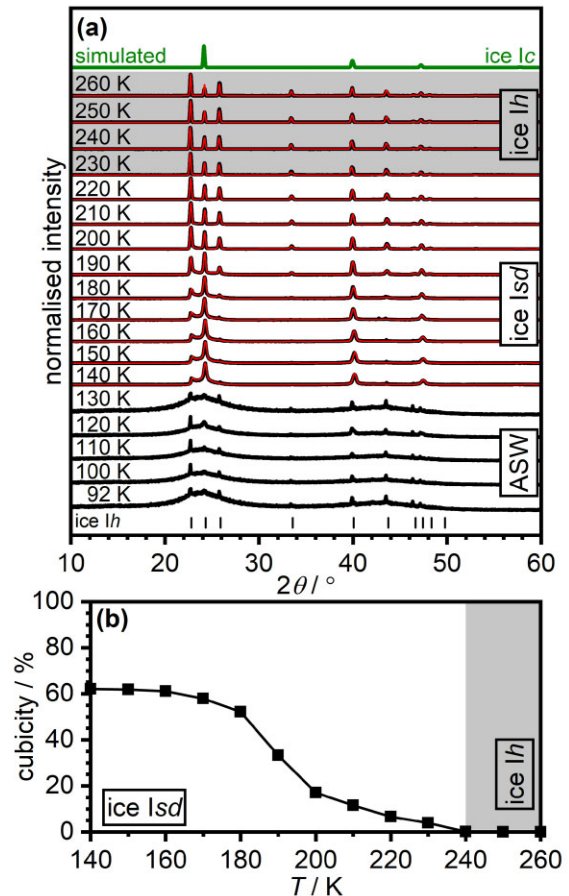

Figure 2. (a) Diffraction patterns collected upon heating ASW at ambient pressure (black). Crystallization to ice Isd is seen by the sharpening of peaks and formation of ice Ih only occurs as the diffuse scattering disappears in the 24–27° range. The red lines indicate MCDIFFAX fits. The tickmarks indicate calculated Bragg reflections of ice Ih. (b) Changes in cubicity of ice Isd with the formation of ice Ih near 240 K.

pressure at 77 K. The broad features at 92 K near 24° and 44° are indicative of LDA (Burton & Oliver [1935b]), and therefore ASW, meaning the ice prepared in the vacuum chamber was successfully extracted and transferred to the diffractometer. Minor impurities of ice Ih can be seen in the shape of sharp Bragg reflections in the ASW data that occur during sample holder transfer from the liquid nitrogen to the CryojetHT as ice Ih condenses into the Kapton windows. Upon heating, as shown previously (Talewar et al. 2019; Halukeerthi et al. [2020]; Li et al. [2021]), ASW crystallizes to ice Isd. If a perfectly crystalline structure was formed, sharper and baseline separated Bragg peaks would be expected. However, this is not observed in Fig. [2](a) until >200K where ice Isd begins to transform to ice Ih. For ice Ih, the baseline separated 'trident' between 23 and 26° is observed, while ice Ic only displays the 24° Bragg peak (del Rosso et al. [2020]; Komatsu et al. [2020]; Salzmann & Murray [2020]) as shown by the simulated ice Ic data in green in panel (a). From this, Fig. [2](a) clearly shows experimental diffraction patterns that are not pure ice Ic, but where the diffuse scattering between the trident peaks indicates stacking disorder. To further analyse the presence of hexagonal and cubic stacking sequences, the diffax software with an added Monte Carlo algorithm (MCDIFFAX) (Salzmann, Murray & Shephard [2015]) was used to fit the X-ray diffraction data in a least-squares environment. To optimize the fit and reach a χ^2 convergence,
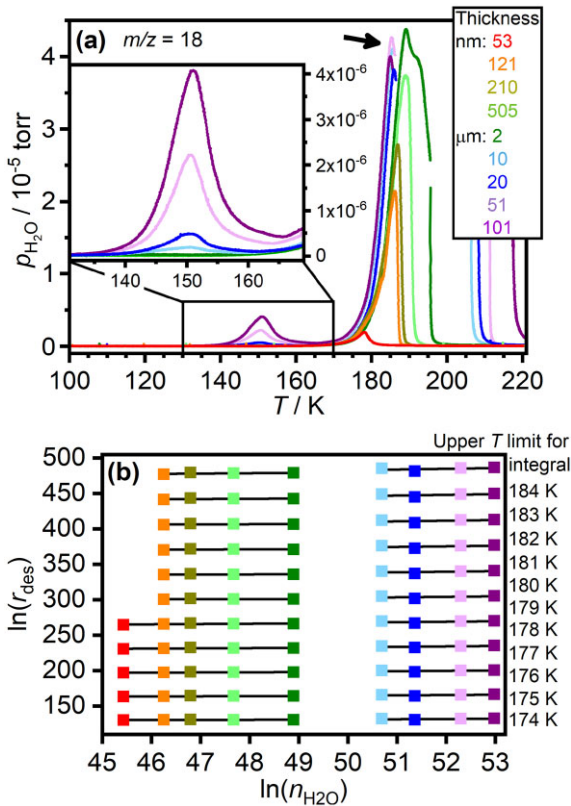
Figure 3. (a) TPD traces of H$_2$O ($m/z = 18$) at increasing film thicknesses ranging from 53 nm to 101 μm. Initially, the traces feature only one desorption event which is split into two separate events at increasing film thicknesses. The insert in (a) highlights the desorption of ASW of the $\geq$10 μm films. The black arrow highlights the drop in partial pressure during ice Isd desorption. (b) Leading-edge analysis indicates zero-order desorption kinetics for all film thicknesses. The colour coding across the two panels indicated H$_2$O film thickness.

the software searches for the best values for the lattice constants, peak profile parameters, and zero-shift, as well as the optimal stacking probabilities. The red lines in Fig. 2(a) are the resultant fits, and from this, the stacking probabilities are obtained including the percentage of cubic stacking events called cubicity shown as a function of temperature in Fig. 2(b). As can be seen, the first pattern of ice Isd only yields a cubicity of 60 percent whereafter the cubicity decreases to zero near 240 K as pure ice Ih forms. From the diffraction data, no other transitions or structural changes are observed, indicating that the 'wiggle' in the QCM data in Fig. 1(b) and the two-stage desorption event in Fig. 1(c) must arise from the ice Isd to ice Ih transition. The minor differences in transition temperatures between the different analytical techniques are due to different heating rates and pressure conditions. However, the overall trend is clear: ASW crystallizes to a stacking disordered ice I, but not to ice Ic.

3.3 Temperature-programmed desorption of H$_2$O

With increasing film thickness, the H$_2$O desorption peak is expected to shift to higher temperatures for adsorbates following zero-order desorption kinetics. The 53 nm thick film has a desorption peak at 178 K, which shifts to $\sim$190 K for the 505 nm film, as seen in Fig. 3(a). These peak temperatures agree well with previous H$_2$O desorption studies of $\sim$40–450 nm H$_2$O films peaking from 178–185 K (Collings et al. 2015; Potapov et al. 2018). It is important

to note that the heating rate also has a considerable impact on the peak temperature at which H$_2$O desorbs, where 11–22 nm films have been observed at $\sim$155–160 K when heating on the K/s scale (Kay et al. 1989; Fraser et al. 2001; Collings et al. 2004; Smith et al. 2011; Salter et al. 2021), which is considerably faster than the heating rates shown in Table 1.

A single desorption event is observed for all film thicknesses up to 2 μm as previously observed for nanometre-scale H$_2$O films (Kay et al. 1989; Fraser et al. 2001; Collings et al. 2004; Smith et al. 2011; Collings et al. 2015; Potapov et al. 2018; Salter et al. 2021). At $\geq$10 μm, a separate ASW desorption feature peaking $\sim$150 K appears and grows with increasing H$_2$O thickness. This desorption feature has previously been observed, but commonly only as a small shoulder near 150 K to the main H$_2$O desorption feature (Smith et al. 2011; Collings et al. 2015; Salter et al. 2021). It is curious to note that ASW desorption is observed for the 10 and 20 μm films in TPD, but not with the QCM in Fig. 1(b and c). The reason for this could simply be due to the mass spectrometer having a greater sensitivity compared to QCM. While there is a slight separation of 2 K in the leading edges between the 2 and 10 μm TPD traces, H$_2$O desorption starting near 170 K display coincident, leading edges on either side of the separation indicative of multilayer desorption following zero-order kinetics shown in Fig. 3(b) and expected for H$_2$O (Collings et al. 2001; Fraser et al. 2001; Smith et al. 2014; Collings et al. 2015). Fig. 3(b) is the result of a leading-edge analysis where the molecules desorbed at certain temperatures are integrated. The gradient of the individual integrals for each TPD trace at a certain temperature determines the kinetic desorption order, which is 0.29 $\pm$ 0.40 in this work. The reason for the shift in the desorption leading edge can be seen in the increased heating rate from 0.64 K min^{-1} for the 2 μm film to 0.73 K min^{-1} for the 10 μm film, Table 1. With increasing amounts of H$_2$O desorbed from the deposition plate, the pressure in the chamber increases, leading to a more effective heat exchange between the chamber walls and the cryostat. This continued bombardment of gas-phase molecules could explain the higher heating rates through convective heating. It is also possible that the increased surface area of the thicker films becomes important for heat exchange. Considering the increased surface area, the greater rates for the $\geq$10 μm film from the onset of heating can be explained as seen in Fig. S2. Following complete desorption of the $\geq$10 μm films, the heating rates drastically decrease, as shown in Fig. S2, to $\sim$0.33 K min^{-1}, lending credence to the notion of increased surface area and chamber pressures raising the substrate heating rate.

The sharp shoulder near 195 K of the 2 μm TPD trace in Fig. 3(a) sets it apart from the thinner film traces where single, clean peaks are displayed. The shoulder in the 2 μm TPD data could indicate the beginning of ice Ih formation upon heating, however, a desorption signal was not observed in Fig. 1(b, c) which may be due to only a small amount of ice Ih being formed and desorbed. As the thickness increases, so does the amount of H$_2$O desorbed and the chamber pressure rises to an extent too great for the safe operation of the mass spectrometer which was temporarily turned off. The diffusion pump and cold trap cannot remove the gas rapidly enough as the 10 and 101 μm films have masses ranging from 0.3 to 3 g. However, before the mass spectrometer is stopped, a drop in the partial pressures of the $\geq$10 μm films is noted near 185 K as highlighted by the black arrow in Fig. 3(a). At this stage the pressure continues to rise due to H$_2$O desorption where Fig. 1(b, c) show that H$_2$O is still present in the solid state. It is therefore likely that the drop in the H$_2$O partial pressure near 190 K is due to the desorption of ice Isd, whereafter ice Ih is formed and begins desorption, leading to the increased chamber
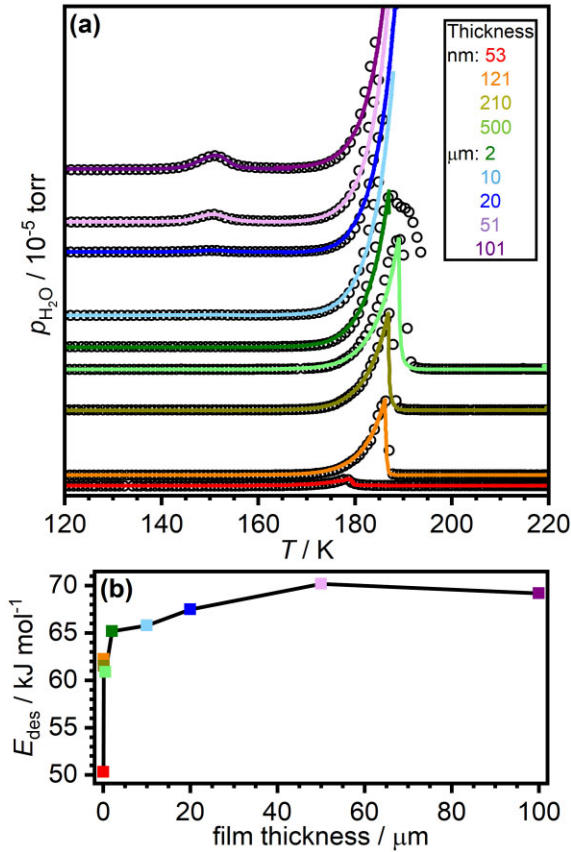
Figure 4. (a) Simulated (solid lines) and experimental data (black open circles) of H_2O desorption. (b) The desorption energy of H_2O as a function of film thickness in micrometres. The colour coding in panel (a) indicates the film thickness.

pressure. The pressure was also recorded during desorption as shown in Fig. S4, which has similar trends to the TPD data in Fig. 3. The pressure increases near 150 K due to ASW desorption, followed by full ice I desorption starting near 170 K with coincident leading edges. Fig. S5 of the $\geq 2\ \mu$m films shows the pressure on a log-scale, which clearly shows a change in pressure near 190 K, coinciding with the temperature of the ice I$sd \rightarrow$Ih transition. The pressure changes in Fig. S5 also indicate that the drop in signal in Fig. 3(a) is real and relates to ice Isd desorption. Following ice Ih desorption of the $\geq 10\ \mu$m films, the chamber pressure decreases rapidly, and the spectrometer was turned on again to collect the trailing desorption edge, highlighting that desorption of the 101 μm film terminates at 220 K, as shown in Fig. 3(a).

3.4 Kinetic simulations of H_2O desorption

The kinetics related to H_2O desorption were simulated with the KINETISCOPE stochastic kinetics simulator (Kinetiscope) and compared to the experimental data, as shown in Fig. 4(a).

The reaction mechanisms in equations (2–4) indicate the physical processes occurring during desorption where *(s)* and *(g)* relate to the physical state of H_2O being solid or gas, respectively, and as such, were used for the KINETISCOPE software.

$$ASW\,(s) \rightarrow H_2O\,(g) \tag{2}$$

$$ice\,I\,(s) \rightarrow H_2O\,(g) \tag{3}$$

$$H_2O\,(g) \rightarrow pump \tag{4}$$
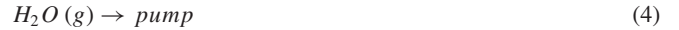
Equation (2) relates to the desorption of ASW, while equation (3) is of ice I desorption and equation (4) is the removal of $H_2O(g)$ by the pump. The initial concentration of *ASW(s)* and *ice I(s)* for the simulations in terms of molecules cm^{-3} were based on the QCM measurements and extrapolated for the area of the entire deposition plate. The recorded data of the heating rates from each individual experiment were loaded directly into KINETISCOPE. The desorption energy (E_{des}) and pre-exponential factor (v) were gathered from an inverse Arrhenius equation shown in equation (5) and used as the initial parameters for the simulation

$$\ln(k) \;=\; \ln(v) \times \frac{-E_{des}}{RT} \tag{5}$$

where k is the rate constant and RT is the product of the ideal gas constant and temperature. The obtained desorption energies from equation (5) are shown in Table 3 alongside the desorption energies and pre-exponential factors extracted from the KINETISCOPE software.

As mentioned previously, a combined peak related to ASW desorption and crystallization commonly occurs during H_2O desorption, however, the separate desorption events shown in Fig. 3(a) are simulated in Fig. 4(a). A best fit with KINETISCOPE leads to an ASW desorption energy of about 64.2 ± 0.3 kJ mol^{-1} and a pre-exponential factor of about $9 \times 10^{17\pm1}$ s^{-1}. This is higher than the 10^{12} s^{-1} typically assumed for physisorbed species, however, it is similar to the 1.1×10^{18} s^{-1} pre-exponential factor for 1000 ML ASW previously determined (Smith et al. 2011). In that study, the desorption energy was determined to be about 55 kJ mol^{-1} (Smith et al. 2011), which is lower than the desorption energy found in this work.

Simulations of the ice I desorption features were also conducted, as shown in Fig. 4(a). The desorption energy and pre-exponential factor of the 53 nm film as shown in Table 3 are in good agreement with the literature (Fraser et al. 2001; Collings et al. 2015; Potapov et al. 2018; Salter et al. 2021). However, as the thickness increases, so does the desorption energy. The desorption energies following the 2 μm film appear to form a plateau in the 64–67 kJ mol^{-1} range. It is important to note that complete ice I desorption data of the >2 μm films could not be collected due to the high chamber pressure during H_2O desorption, however, the leading edges have been simulated to the best extent possible in Fig. 4(a). The average desorption energy (65.3 kJ mol^{-1}) and pre-exponential factor (2×10^{34} molecules cm^{-2} s^{-1}) being greater than the literature (commonly found to be near 50 kJ mol^{-1} and 10^{28}–10^{30} molecules cm^{-2} s^{-1}; Fraser et al. 2001; Collings et al. 2015; Potapov et al. 2018) will be discussed later.

4 ASTROPHYSICAL IMPLICATIONS

Investigating the kinetics of physical processes, such as desorption, is of crucial importance for furthering our understanding of the astrophysical environment as recently discussed in a detailed review (Minissale et al. 2022). As H_2O is the most abundant solid in the interstellar medium, it has attracted a lot of attention and been thoroughly studied. However, the thick film/bulk H_2O desorption behaviour reported here has so far not been investigated.

With increasing thickness, desorption processes for ASW and ice Isd are shown to be separated by 10–15 K. The QCM data quantifies the H_2O loss during crystallization to be $\sim$4 percent for a 101 μm thick film heated at $\sim$1 K min^{-1}. This means that upon crystallization

Table 3. The initial estimate of the desorption energies from an inverse Arrhenius analysis are in line with the extracted parameters gathered from the KINETISCOPE software which also yields the pre-exonential factors.

Film thickness	Inverse Arrhenius analysis/kJ mol^{-1}	E_{des}/kJ mol^{-1}	ν_{des}/molecules cm^{-2} s^{-1}
53 nm	48	50.3	1×10^{30}
100 nm	59	62.2	1×10^{30}
210 nm	61	61.5	1×10^{30}
500 nm	63	60.9	1×10^{30}
2 μm	64	65.2	1×10^{32}
10 μm	67	65.8	1×10^{33}
20 μm	67	67.5	5×10^{33}
51 μm	66	70.2	1×10^{35}
101 μm	66	69.2	1×10^{35}

of ASW, H_2O-ice in an astrophysical environment may only lose a small amount of mass during crystallization, but this will be dependent on the heating rate. Considering approximate heating rates in hot cores of 1 K century^{-1} or 1 K per 100 centuries as estimated for protostellar environments (Viti et al. 2004), it is probable that complete crystallization occurs without desorption of ASW. The heating rates of comets and asteroids, on the other hand, are complex to estimate due to factors such as distance from a stellar object, presence of coma, albedo, and rotation about their axis. The surface temperature of the asteroid Steins was estimated as ranging between 185 and 225 K during rotation about its axis as measured with the VIRTIS instrument during a flyby of the Rosetta mission (Leyrat et al. 2011). Similarly, the surface temperature of 67P/Churyumov–Gerasimenko measured by the VIRTIS instrument reached upwards of 230 K at a distance of 3.31 and 3.62 au from the Sun (Tosi et al. 2019). During the full diurnal rotation period (about 88 min), the temperature changes at least 65 K, leading to a heating rate of ∼0.78 K min^{-1}, however, the VIRTIS instrument has a threshold for measuring temperature below 160 K, meaning that the 0.78 K min^{-1} heating rate is an upper estimate. At such heating rates, ASW is expected to desorb if present on the surface. As 67P/Churyumov–Gerasimenko is known to have a rough and uneven surface, the temperature of areas leaving a shaded area are thought to change by ∼9 K min^{-1} (Tosi et al. 2019), which would rapidly desorb ASW. The surface temperature of 67P/Churyumov–Gerasimenko has not been measured at perihelion, but the nucleus temperature has been estimated at >180 K (Huebner et al. 2006). The difference in surface and core temperatures is due to the insulating properties of the coma and ice of comets and asteroids as also studied for Halley's comet at perihelion where the nucleus could reach 496 K without coma and ice desorption (Weissman & Kieffer 1984), compared to ∼210 K with a coma and ice (Kührt 1984; Weissman & Kieffer 1984).

As ASW crystallizes, ice Isd forms and not ice Ic as commonly stated. The conversion from ASW to ice Isd and later to ice Ih are all irreversible upon heating. However, amorphization of ice I through energetic processing, such as proton, ion, and molecular bombardment, can still occur (Baratta et al. 1991; Moore & Hudson 1992; Leto & Baratta 2003; Rosu-Finsen & McCoustra 2018). Aside from direct physisorption of ice Ih (believed to be a minor part of ice build-up), the formation of ice Ih from ice Isd occurs 10–15 K before full desorption for the ≥10 μm thick films. Therefore, it is possible that the main ice I polymorph found in the interstellar medium is ice Isd existing over a 40–50 K range. The spectral differences between ice Isd, Ic, and Ih have previously been investigated through Raman spectroscopy, and a red-shift in the O-H stretch has been noted as ice Isd is heated to ice Ih, which could be of interest to the astronomical community (Carr, Shephard & Salzmann 2014; del Rosso et al. 2020).

Full ice Ih desorption is not observed until 220 K for the 101 μm thick film studied here. Any guest species still trapped within an ice I matrix following crystallization would only co-desorb with ice I. As full ice I desorption is first reached near 220 K with the heating rate used here, this gives thick H_2O films the potential to act as a molecular sink retaining species at increasing temperatures, which would otherwise have been released into the gas-phase.

5 CONCLUSIONS

The peak of ASW desorption is found near 150 K with a desorption energy of 64.2 kJ mol^{-1} and a pre-exponential factor 9×10^{17} s^{-1} where ∼4 percent of the H_2O molecules desorb for the 101 μm film. This desorption energy is smaller than that of ice I due to the differences in free energy and vapour pressure.

Following crystallization, the X-ray diffraction patterns clearly show the formation of ice Isd and not the commonly mentioned ice Ic. Coupled with QCM and TPD, the X-ray diffraction patterns show that the two-stage desorption in Fig. 1(c), the drop in partial pressures in Fig. 3(a), and the changes in pressure shown in Fig. S5 relate to the desorption of ice I sd followed by ice Ih at higher temperatures. There is a 40–50 K temperature range between ASW desorption and the ice Isd→Ih transition, meaning that a significant amount of crystalline ice I in the astrophysical environment is expected to be ice Isd.

Ice Isd desorption starts near 170 K. The desorption kinetics of the 53 nm film in this work matches those reported for thin films studied in ultrahigh vacuum conditions with a desorption energy near 50 kJ mol^{-1} and pre-exponential factor near 10^{30} molecules cm^{-2} s^{-1}. However, with increasing amounts of H_2O, the desorption energy increases rapidly up to about 64–67 kJ mol^{-1} where a plateau is reached as shown in Fig. 4(b). The large increase in desorption energy is due to the increase in film thicknesses where the above-layered H_2O molecules act as a physical barrier for the desorbing molecules. Depending on the temperature, thermally activated but physically trapped molecules can re-adsorb forming ice Ih. As such, the H_2O-vacuum-interfacing molecules only desorb once the heat has been transmitted through the bulk of the ice. Eventually the entire film desorbs, leading to the apparent desorption energies stated in this work. As H_2O is known to be a good thermal insulator, this transfer takes time where delays in desorption of reaction products or guest species have previously been mentioned for H_2O films (Gadallah et al. 2017; Jiménez-Escobar et al. 2022).

When modelling the effect of radiative heating on the desorption of thick icy layers (Rubanenko & Aharonson 2017; Davidsson and Hosseini 2021), the parameters extracted from desorption experiments are crucial. As radiative heating affects the ice-vacuum interface,

the desorption parameters of thin H_2O films found in the literature are ideal. However, in the event of grain core heating [e.g. Ohmic heating from strong magnetic sources (Bromley & Kenyon 2019)] or exothermic reactions releasing energy in a H_2O matrix, the energy typically thought to lead to H_2O desorption can be revised to consider film thickness. As H_2O thicknesses vary, the desorption energy increases by up to 30 percent compared to what is typically reported in the literature meaning that models need to include a desorption energy relevant to the type of heating and film thickness.

ACKNOWLEDGEMENTS

DATA AVAILABILITY

The data produced in this paper will be shared on reasonable request to the corresponding author.

REFERENCES

Aumatell G., Wurm G., 2011, MNRAS, 418, L1
Baratta G.A., Leto G., Spinella F., Strazzulla G., Foti G., 1991, A&A, 252, 421
Boogert A. et al., 2008, ApJ, 678, 985
Boogert A. et al., 2011, ApJ, 729, 92.
Bromley B. C, Kenyon S. J., 2019, ApJ, 876, 17
Brüggeller P., Mayer E., 1980, Nature, 288, 569
Burton E. F., Oliver W. F., 1935a, Proc. R. Soc. London, Ser. A, 153, 166
Burton E. F., Oliver W. F., 1935b, Nature, 135, 505
Carr T. H., Shephard J. J., Salzmann C. G., 2014, J. Phys. Chem. Lett., 5, 2469
Carrasco J., Hodgson A., Michaelides A., 2012, Nature Mater., 11, 667
Collings M. P., Dever J. W., Fraser H. J., McCoustra M. R. S., Williams D. A., 2003, ApJ, 583, 1058
Collings M. P., Frankland V. L., Lasne J., Marchione D., Rosu-Finsen A., McCoustra M. R. S., 2015, MNRAS, 449, 1826
Collings M. P., Anderson M. A., Chen R., Dever J. W., Viti S., Williams D. A., McCoustra M. R. S., 2004, MNRAS, 354, 1133
Collings M. P., McCoustra M. R. S., Fraser H. J., Williams D. A., 2001, MNRAS, 327, 1165
Davidsson B. J. R., Hosseini S., 2021, MNRAS, 506, 3421
De Sanctis M. C. et al., 2015, Nature, 525, 500
del Rosso L., Celli M., Grazzi F., Catti M., Hansen T. C., Fortes A. D., Ulivi L., 2020, Nature Mater., 19, 663
Dohnálek Z., Kimmel G. A., Ayotte P., Smith R. S., Kay B. D., 2002, J. Chem. Phys., 118, 364
Filacchione G. et al., 2016, Nature, 529, 368
Fraser H. J., Collings M. P., McCoustra M. R. S., Williams D. A., 2001, MNRAS, 327, 1165
Gadallah K. A. K., Marchione D., Koehler S. P. K., McCoustra M. R. S., 2017, Phys. Chem. Chem. Phys., 19, 3349
Gärtner S. et al., 2017, ApJ, 848, 96
Gibb E. L., Whittet D. C. B., Boogert A. C. A., Tielens A. G. G. M., 2004, ApJ Suppl. Series, 151, 35
Grundy W. M. et al., 2016, Science, 351, 1283
Gundlach B., Blum J., 2014, ApJ, 798, 34
Halukeerthi S. O., Shephard J. J., Talewar S. K., Evans J. S. O., Rosu-Finsen A., Salzmann C. G., 2020, J. Phys. Chem. A, 124, 5015
Hatzes A. P., Bridges F., Lin D. N. C., Sachtjen S., 1991, Icarus, 89, 113
Heißelmann D., Blum J., Fraser H. J., Wolling K., 2010, Icarus, 206, 424

Hill C. R., Heißelmann D., Blum J., Fraser H. J., 2015, A&A, 573, A49
Hill C. R., Mitterdorfer C. A., Youngs T. G., Bowron D. T., Fraser H. J., Loerting T., 2016, Phys. Rev. Lett., 116, 215501
Huebner W. F., Benkhoff J., Capria M.-T., Coradini A., de Sanctis C., Orosei R., Prialnik D., 2006, Scientific Report 004, Heat and Gas Diffusion in Comet Nuclei. International Space Science Institute, Bern, Switzerland
Jenniskens P., Blake D. F., 1994, Science, 265, 753
Jiménez-Escobar A., Ciaravella A., Cecchi-Pestellini C., Muñoz Caro G. M., Huang C.-H., Sie N.-E., Chen Y.-J., 2022, ApJ, 926, 176
Kay B. D., Lykke K. R., Creighton J. R., Ward S. J., 1989, J. Chem. Phys., 91, 5120
Kimmel G. A., Stevenson K. P., Dohnálek Z., Smith R. S., Kay B. D., 2001, J. Chem. Phys., 114, 5284
Kinetiscope, https://hinsberg.net/kinetiscope/[accessed 08/10/2022]
Klug D. D., Handa Y. P., Tse J. S., Whalley E., 1989, J. Chem. Phys., 90, 2390
Komatsu K., Machida S., Noritake F., Hattori T., Sano-Furukawa A., Yamane R., Yamashita K., Kagi H., 2020, Nature Commun., 11, 464
Korsmeyer J. M., Ricca A., Cruz-Diaz G. A., Roser J. E., Mattioda A. L., 2022, ACS Earth Space Chem., 6, 165
Kouchi A., Greenberg J. M., Yamamoto T., Mukai T., 1992, ApJ, 388, L73
Kouchi A., 1987, Nature, 330, 550
Kührt E., 1984, Icarus, 60, 512
Kuhs W. F., Bliss D. V., Finney J. L., 1987, J. Phys. Colloq., C1, 48, 631
Kuhs W. F., Sippel C., Falenty A., Hansen T. C., 2012, Proc. Natl. Acad. Sci., 109, 21259
Leto G., Baratta G. A., 2003, A&A, 397, 7
Leyrat C., Coradini A., Erard S., Capaccioni F., Capria M. T., Drossart P., De Sanctis M. C., Tosi F., VIRTIS Team, 2011, A&A, 531, A168
Li H., Karina A., Ladd-Parada M., Späh A., Perakis F., Benmore C., Amann-Winkel K., 2021, J. Phys. Chem. B, 125, 13320
Linnartz S., Ioppolo S., Fedoseev G., 2015, Int. Rev. Phys. Chem., 34, 205
Lisitsin-Baranovsky E., Delage S., Sucre O., Ofer O., Ayotte P., Alexandrow-icz G., 2016, J. Phys. Chem. C, 120, 25445
Malkin T. L., Murray B. J., Salzmann C. G., Molinero V., Pickering S. J., Whale T. F., 2015, Phys. Chem. Chem. Phys., 17, 60
Marchione D. et al., 2019, ACS Earth Space Chem., 3, 1915
Mathis J. S., Rumpl W., Nordsieck K. H., 1977, ApJ, 217, 425
May R. A., Smith R. S., Kay B. D., 2012, J. Phys. Chem. Lett., 3, 327
Mayer E., Brüggeller P., 1982, Nature, 298, 715
Mayer E., Hallbrucker A., 1989, J. Am. Chem. Soc., 12, 749
Mayer E., Pletzer R., 1984, J. Chem. Phys., 80, 2939
McDonald J. S. B., Hatzes A., Bridges F., Lin D. N. C., 1989, Icarus, 82, 167
Minissale M. et al., 2022, ACS Earth Space Chem., 6, 597
Mishima O., Calvert L. D., Whalley E., 1984, Nature, 310, 393
Mishima O., Calvert L. D., Whalley E., 1985, Nature, 314, 76
Mitterdorfer C., Bauer M., Youngs T. G. A., Bowron D. T., Hill C. R., Fraser H. J., Finney J. L., Loerting T., 2014, Phys. Chem. Chem. Phys., 16, 16013
Moore M. H., Hudson R. L., 1992, ApJ, 401, 353
Nachbar M., Duft D., Leisner T., 2018, Atmos. Chem. Phys., 18, 3419
Narten A. H., Venkatesh C. G., Rice S. A., 1976, J. Chem. Phys., 64, 1106
Potapov A., Bouwman J., Jäger C., Henning T., 2021, Nature Astron., 5, 78
Potapov A., Jäger C., Henning T., 2018, ApJ, 865, 58
Potapov A., Jäger C., Henning T., 2020, Phys. Rev. Lett., 124, 221103
Rosu-Finsen A., McCoustra M. R. S., 2018, Phys. Chem. Chem. Phys., 20, 5368
Rosu-Finsen A., Marchione D., Salter T. L., Stubbing J. W., Brown W. A., McCoustra M. R. S., 2016, Phys. Chem. Chem. Phys., 18, 31930
Rubanenko L., Aharonson O., 2017, Icarus, 296, 99
Sack N. J., Baragiola R. A., 1993, Phys. Rev. B, 48, 9973
Salter T. L., Stubbing J. W., Brigham L., Brown W. A., 2021, Front. Astron. Space Sci., 8, 644277
Salzmann C. G., Murray B. J., 2020, Nature Mater., 19, 586
Salzmann C. G., Murray B. J., Shephard J. J., 2015, Diam. Relat. Mater., 59, 69
Shephard J. J., Evans J. S. O., Salzmann C. G., 2013, J. Phys. Chem. Lett., 4, 3672

Shephard J. J., Klotz S., Vickers M., Salzmann C. G., 2016, J. Chem. Phys., 144, 204502

Smith R. S., Matthiesen J., Knox J., Kay B. D., 2011, J. Phys. Chem. A, 115, 5908

Smith R. S., Huang C., Wong E. K. L., Kay B. D., 1997, Phys. Rev. Lett., 79, 909

Smith R. S., Matthiesen J., Kay B. D., 2014, J. Phys. Chem. A, 118, 8242

Smith R. S., Petrik N. G., Kimmel G. A., Kay B. D., 2012, Acc. Chem. Res., 45, 33

Stevenson K. P., Kimmel G. A., Dohnalek Z., Smith R. S., Kay B. D., 1999, Science, 283, 1505

Talewar S. K. et al., 2019, J. Chem. Phys., 151, 134505

Tielens A. G. M., 2013, Rev. Mod. Phys., 85, 1021

Tosi F. et al., 2019, Nature Astron., 3, 649

Viti S., Collings M. P., Dever J. W., McCoustra M. R. S., Williams D. A., 2004, MNRAS, 354, 1141

Wada K., Tanaka H., Suyama T., Kimura H., Yamamoto T., 2009, ApJ, 702, 1490

Weissman P. R., Kieffer H. H., 1984, J. Geophys. Res. Solid Earth, 89, C358

Williams D. A., Fraser H. J., McCoustra M. R. S., 2002, Astron. Geophys., 43, 2.10

Winkel K., Bowron D. T., Loerting T., Mayer E., Finney J. L., 2009, J. Chem. Phys., 130, 204502

SUPPORTING INFORMATION

Supplementary data are available at *MNRAS* online.

SI.docx

Please note: Oxford University Press is not responsible for the content or functionality of any supporting materials supplied by the authors. Any queries (other than missing material) should be directed to the corresponding author for the article.

This paper has been typeset from a TEX/LATEX file prepared by the author.